Adaptive ensemble PTV

Marco Raiola[1], Elena Lopez-Nuñez[2], Gioacchino Cafiero[3] and Stefano Discetti[1]

[1] Aerospace Engineering Research Group, Universidad Carlos III de Madrid (UC3M), Av.da Universidad, 30, 28911 Leganes, Madrid, Spain
[2] Instituto Universitario de Microgravedad Ignacio da Riva, Universidad Politécnica de Madrid, E.T.S.I. Aeronáutica y del Espacio, Plaza Cardenal Cisneros 3, 28019, Madrid, Spain
[3] Department of Mechanical Engineering Sciences, University of Surrey, Guildford, GU2 7HX, UK

E-mail: `sdiscett@ing.uc3m.es`

Abstract. Ensemble Particle Tracking Velocimetry (EPTV) is a method to extract high-resolution statistical information on flow fields from Particle Image Velocimetry (PIV) images. The process is based on tracking particles and extracting the velocity probability distribution functions of the image ensemble in averaging-regions deemed to contain a sufficient number of particle pairs/tracks. The size of the averaging regions depends on the particle density and the number of snapshots. An automatic adaptive variation of the ensemble PTV is presented to further push the spatial resolution of the method. The proposed Adaptive-EPTV is based on stretching and orienting the averaging regions along the direction of maximum curvature of the velocity fields. The process requires a predictor calculation with isotropic-window EPTV to compute the second derivatives of the mean velocity components. In a second step, the principal directions of the Hessian tensor are calculated to tune the optimal orientation and stretch of the averaging regions. The stretching and orientation are achieved using a Gaussian windowing with different standard deviation along the local principal direction of the Hessian tensor. The algorithm is first validated using three different synthetic datasets: a sinusoidal displacement field, a channel flow and the flow around a NACA 0012 airfoil. An experimental test case of an impinging jet equipped with a fractal grid at the nozzle outlet is also carried out.

Submitted to: *Meas. Sci. Technol.*

1. Introduction

A long-standing line of research in Particle Image Velocimetry (PIV) is devoted to increase its capabilities in terms of spatial resolution. Traditionally, the focus has been on two lines:

- maximize the spatial resolution of instantaneous measurements: to cite some, the advanced multi-step multi-grid [1] image deformation algorithms [2], the adaptive PIV concept [3, 4, 5] and several methods to pour time resolution into space [6, 7, 8];
- maximize the spatial resolution of turbulent statistics, exploiting ensemble information to push the resolution beyond the limits of the instantaneous measurements.

Along this second path, the first approaches were correlation-based, starting with the pioneering work by Meinhart et al. [9], introducing the ensemble-correlation concept. The method was based on summing correlation maps to pump up the coherent signal related to the mean velocity field. While this approach was originally conceived for micro-PIV applications [10], the concept was later extended to turbulent flows and referred to as *single-pixel* resolution [11]. Exploiting the statistical stationarity of the measurement process as an additional source of information, the spatial resolution can be brought ideally down to a single pixel.

This approach has been extended to deliver second-order statistics from the deconvolution of the ensemble-correlation maps [12], as well as for the application in unsteady flows [13] and in stereoscopic measurements [14]. Nonetheless, ensemble-correlation has issues with slow convergence, which can be partly mitigated using symmetric double correlation [15]. Additionally, the computational burden and memory requirements hinder the application of ensemble correlation to 3D PIV, in which instead approaches based on 3D Ensemble Particle Tracking Velocimetry (EPTV) have been gaining increasing popularity [16].

EPTV is based on collecting particle pairs/tracks to create a dense ensemble, whose density can be increased virtually without limit. Turbulence statistics at high resolution are obtained extracting the probability distribution function (pdf) of the velocity vectors in each averaging bin. This concept was introduced by Cowen and Monismith [17] as a hybrid digital PTV, exploiting cross-correlation as a predictor for particle pairing as in the super-resolution PIV [18]. EPTV received limited attention for almost 25 years, being it obscured by the superiority of cross-correlation approaches. The interest in PTV, and consequently in extracting high-resolution statistics from scattered vectors, raised quickly in recent years driven by the outstanding developments of 3D Lagrangian Particle Tracking [19, 20].

The group of Kähler at UNIBW [21] built the underpinnings of a renaissance of PTV also for planar applications, demonstrating that the actual resolution limit of single-pixel correlation is related to the particle image diameter; PTV, on the other hand, is not limited by the typical issues of cross-correlation, such as the filtering effect of the diffraction spot, background noise and bias of laser reflections. This leads to a much superior performance in terms of dynamic range of the turbulence statistics. The diameter of the averaging area is defining the spatial resolution, and it can be reduced in size (at fixed number of particles) simply by increasing the number of samples. Ideally, the spatial resolution can be pushed even below the pixel.

This concept has been brought to 3D in recent applications ([22, 23, 24, 25]) with evident gain in terms of computational cost if compared to ensemble correlation. Additionally, EPTV is of straightforward implementation for methods providing output directly in form of particles pairs or tracks, as in the state-of-art shake-the-box method [20]. Nonetheless, depending on the desired bin size, the number of snapshots required might be often prohibitive.

Considering a 2D PIV experiment, to achieve single-pixel resolution of the turbulence statistics with EPTV, the number of snapshots $N_{img_{2D}}$ needed is:

$$N_{img_{2D}} = \frac{N_p}{b^2 N_{ppp}} \tag{1}$$

where N_p is the number of particles needed in each bin to achieve sufficient convergence of the statistics, b is the linear bin size (supposed square for simplicity) and N_{ppp} is the particle image density expressed in particles per pixel. If $b = 1$ pixel and $N_{ppp} = 0.05$, this leads to 10000 snapshots to obtain $N_p = 500$ particles on average in each bin. In 3D:

$$N_{img_{3D}} = \frac{N_p L_z}{b^3 N_{ppp}} = \frac{N_p N_{g,z}}{b^2 N_{ppp}} = N_{img_{2D}} N_{g,z} \tag{2}$$

where L_z is the depth of the reconstructed volume discretized with the same resolution of the images, and $N_{g,z} = b/L_z$ is the number of independent grid points in the depth direction. Considering a quite common case of volume observed by 1Mpixel cameras and volume aspect ratio of 5:1 between in-plane and depth direction, $N_{g,z} = 200$ points and for the same case presented above, 2 million snapshots are needed to reach convergence. This leads, inevitably, to sacrifice the resolution in terms of bin size b.

Agüera et al. [26] observed that, if velocity gradients are not adequately resolved, the residual unresolved velocity gradient contaminates also the

Reynolds stresses computation. For this reason, they proposed an innovative approach with polynomial fitting of the cloud of particles extracted in each averaging box. This approach surprisingly allows to follow wavelengths of the order of the averaging box size and to dramatically reduce the contamination of the Reynolds stresses due to unresolved mean velocity gradients. This allows maintaining a rather large bin size b and still enjoying the resolution of an equivalent smaller bin. With this approach Agüera et al. [26] reduced the requirement on the number of samples ideally up to 27 times in 3D applications.

All the aforementioned methods employ isotropic averaging bins. Nonetheless, there are several cases where an obvious choice of elongated bins can be employed to exploit flow anisotropy and increase the resolution in the directions where the largest velocity differences occur. In turbulent wall-bounded flows, for instance, elongated bins in the wall-parallel direction clearly allow to maintain the same averaging area/volume (thus ideally the same number of particles per bin) with smaller bin size in the wall-normal direction and, consequently, to improve the resolution in this direction (see e.g. Refs. [27, 28]). For instantaneous fields, Di Florio et al. [29] proposed to stretch the interrogation windows according to the local direction of the velocity. Later, Scarano [30] proved that an optimal stretching should be based on the second derivative of the velocity fields. Nonetheless, methods aiming to reduce the velocity difference inside the interrogation window (either based on velocity [29] or velocity-gradient direction [5]) have the advantage of increasing the signal-to-noise ratio of cross-correlation maps. Methods based on the Hessian of the velocity fields [3, 30] are more rigorously adapting the interrogation window to minimize the modulation effect on velocity profiles due to averaging; on the downside, the difficulty in achieving robust measurements of second derivatives hinders the application to instantaneous fields. Astarita [4] proposed to overcome this issue using the even part of the fluctuating velocity field, which is a more robust indicator of a modulation effect due to velocity-profile curvature. However, methods based on the Hessian have shown some success in adaptive processes based on ensemble fields, where the computation of second derivatives is significantly more robust [31].

In this work, we propose a novel Adaptive Ensemble PTV (A-EPTV), conceptually similar to the solution proposed by [31], but with the advantage of a much slender implementation when combined with the EPTV approach. The unnecessary requirement of isotropic averaging can be suppressed by locally adapting the averaging bin in a recursive process. A predictor field is estimated using the high-resolution polynomial-fit method proposed by Agüera et al. [26]; the predictor is used to determine a local stretching magnitude and direction for the averaging bins.

The working principle of the Adaptive Ensemble PTV is presented in §2. A validation of the method with 2D synthetic images of a 1D sinusoidal displacement, a turbulent channel flow and the flow around a NACA0012 airfoil is presented in §3. An experimental application of the method to a jet flow with a fractal grid located at the nozzle outlet is reported in §4. Finally, in §5 the main conclusions of the study are shown.

2. Working principle of the Adaptive Ensemble PTV

The proposed algorithm, sketched in Figure 1, can be subdivided into two main phases: 1) predictor estimation and 2) window adaptation. The first part of the process coincides with the EPTV procedure as described by Agüera et al. [26] and briefly described here for both 2D and 3D cases.

The first step of the process is the identification of the particles position. For a standard planar PIV, it consists in identifying local maxima and interpolate to achieve sub-pixel accuracy (e.g. with Gaussian interpolation [32] or wavelet-based algorithms [33]). For volumetric PIV, there is a wealth of methods to obtain particle positions, including, among others, standard multi-camera triangulation [34], digital defocusing [35], tomographic PTV [36, 37], iterative particle reconstruction [19] and shake-the-box [20].

The particle pairs should be matched between subsequent exposures. For 2D applications a super-resolution approach [17, 18] might be required to increase the robustness. In time-resolved applications, further constraints can be enforced to build particle tracks, e.g. time consistency and trajectory smoothness [38, 39]. In 3D, since the particle spacing is larger than in planar PIV, the choice of the matching algorithm is less critical. Nonetheless, it is clear that, if time-resolution is available, an improvement in reconstruction quality can be obtained with an intense cross-talk between particle identification and matching [20].

Once the velocity vectors corresponding to each snapshot are available, ensemble averages are performed in bins. The bin size is selected according to the number of samples and the number of particles desired in each spot to achieve satisfactory convergence. The local pdf of the velocity components can be extracted from the statistical dispersion of the velocity field itself. The averaging procedure can be based on top-hat weighting or using a filtering approach [26].

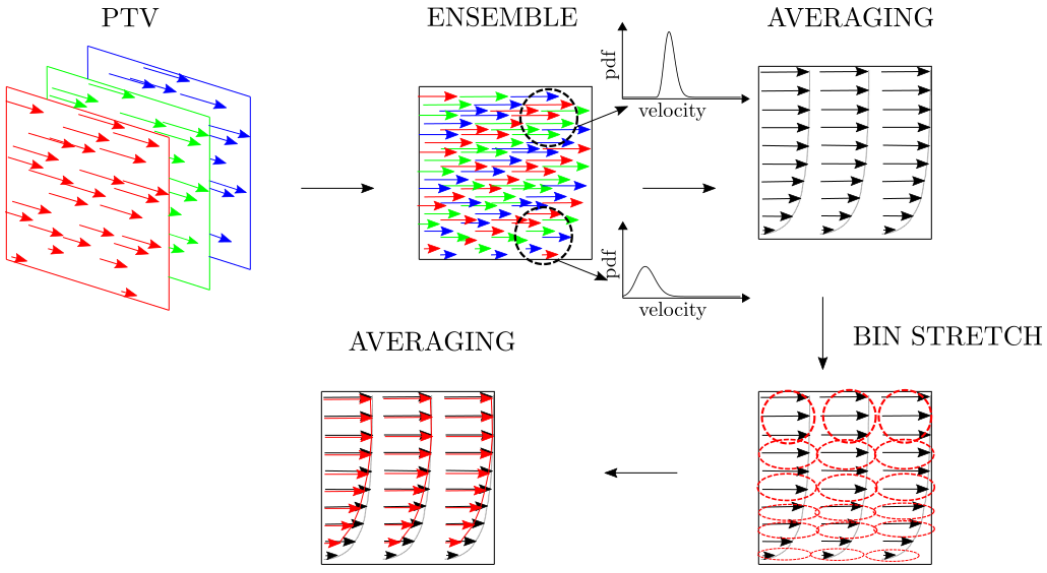

Figure 1. Schematic chart of the Adaptive Ensemble PTV process.

The second phase of the algorithm is the automatic adaptive stretching of the bins. In this work, a procedure similar to the one proposed by Scarano for instantaneous fields [30] is implemented. The process is based on stretching the windows according to the direction with the largest curvature of the velocity components.

For this purpose, the Hessian tensor $\boldsymbol{H}$ is constructed using the predictor obtained from the standard EPTV (i.e. with isotropic window). In this implementation the Hessian tensor is calculated separately for each velocity component, thus providing different stretching direction for each of them. A Savitzky-Golay filtering with a 2^{nd} order polynomial function on a 5×5 kernel is performed to reduce noise effects in the computation of the second derivative. As proposed by Novara et al. [5] for the velocity gradient, an eigendecomposition in each grid point is performed to identify the principal directions of the Hessian tensor, i.e. to spot the directions of minimum and maximum curvature for each of the velocity components:

$$\mathbf{H} = \begin{bmatrix} \frac{\partial^2 u}{\partial x^2} & \frac{\partial^2 u}{\partial x \partial y} & \frac{\partial^2 u}{\partial x \partial z} \\ \frac{\partial^2 u}{\partial y \partial x} & \frac{\partial^2 u}{\partial y^2} & \frac{\partial^2 u}{\partial y \partial z} \\ \frac{\partial^2 u}{\partial z \partial x} & \frac{\partial^2 u}{\partial z \partial y} & \frac{\partial^2 u}{\partial z^2} \end{bmatrix} = \mathbf{BSB}^* \qquad (3)$$

with $\boldsymbol{S}$ being a diagonal matrix containing the eigenvalues of $\boldsymbol{H}$, sorted according to their intensity. The columns of the matrix $\boldsymbol{B}$ are the eigenvectors of the decomposition, which corresponds to the principal directions of the curvature along which the bins are stretched. The ratios of the eigenvalues are indicators of the anisotropy of the curvature, and consequently the stretching ratio should be set according to their value. Following previous works [3, 5], this stretching process can be easily implemented using an anisotropic Gaussian function to weight the contribution of each vector to the turbulence statistics:

$$w(x,y,z) = \exp\left(\sum_{i=1}^{N} \frac{d_i^2(x,y,z)}{2\sigma_i^2}\right) \qquad (4)$$

where $w(x,y,z)$ are the weights, N is the number of the dimension of the space (2 for planar EPTV, 3 for volumetric EPTV), d_i are the distances (along the principal directions of $\mathbf{H}$) of each vector position in the ensemble from the grid point, and σ_i is the standard deviation of the Gaussian in each principal direction. The values of σ_i are set according to the local anisotropy of the second derivative. Following the criteria set by Novara et al. [5] for the velocity-gradient stretching, for the general application to the Hessian in 3D:

$$\sigma_1 = \frac{\sigma_0}{\sqrt[3]{AR_{31}AR_{21}}} \qquad (5)$$

$$\sigma_2 = \sigma_1 AR_{21} \qquad (6)$$

$$\sigma_3 = \sigma_1 AR_{31} \qquad (7)$$

where 1, 2 and 3 are the principal directions (sorted for decreasing corresponding singular value), AR_{31} and AR_{21} are the elongation ratios along the direction 2 and 3 with respect to the direction 1, and σ_0 is the spherical Gaussian window width for isotropic analysis

(i.e. selected to achieve a weight equal to e^{-1} at the edge of the averaging bin). For 2D application, the same relations hold with $AR_{31} = 1$.

The aspect ratios are then computed as [5]:

$$AR_{n1} = (AR_{max} - 1 + \varepsilon)\left(1 - \frac{s_n}{s_1}\right) + 1 \qquad (8)$$

where s_n is the eigenvalue for the n^{th} direction, AR_{max} is the maximum aspect ratio and ε is a parameter which set the aspect ratio to the maximum value when s_n/s_1 falls below a certain threshold. Novara et al. [5] set $\varepsilon = 0.3$ for the velocity-gradient stretching, which locks the limit ratio for s_n/s_1 at 0.1 for $AR_{max} = 4$. The same criteria is applied here for the stretching based on the Hessian.

An additional threshold has been implemented on the minimum curvature of the velocity profile which triggers the adaptive algorithm by imposing bin stretching only if $s_{max} = \max(s_1, s_2, s_3) \geq 1/b^2$, being b the bin size. This condition can be obtained by considering that, if the second derivatives are computed numerically on a three-point stencil with size b (i.e. with grid points spaced by $b/2$), with a minimum detectable difference of 0.1 pixels displacements, the order of magnitude of the second derivative is $2{\cdot}0.1/(b/2)^2 \approx \mathcal{O}(1/b^2)$. This set of parameters has been used throughout the paper.

The process can, in principle, be iterated to improve the computation of the second derivatives and thus the reliability of the windows stretching procedure. Nonetheless, in our experience, the algorithm produces only marginal improvements when iterated, thus all the results presented in the following have been obtained with one direct execution of the process.

It has to be underlined that this method reduces the modulation effects due to the curvature, but the detrimental effect of unresolved velocity gradients are still present in the window and contaminate the estimation of turbulent statistics. Consequently, for second order-statistics the filtering approach proposed by Agüera et al. [26] is still highly recommended and used throughout this work.

3. Validation

3.1. 1D Sinusoidal displacement fields

The algorithm is validated on 2D synthetic images of a 1D sinusoidal displacement with variable wavelength. A set of 500 image pairs is generated, with particle image density of 0.01 particles per pixel and size of 640×640 pixels. The particle images are generated by the integration of Gaussian spots with diameter equal to 3 pixels and maximum intensity of 100 counts. The pixel fill-factor is set equal to 1.

The simulated displacement field is:

$$u(x, y) = \sin\left(\frac{2\pi y}{\lambda}\right) \qquad (9)$$

with λ being the wavelength of the displacement, x, y being the horizontal and vertical directions, respectively, and u being the velocity component in the x direction. The sinusoidal test has been extensively used in PIV to determine the Modulation Transfer Function (MTF) of the algorithm, thus giving a straightforward evaluation of the spatial resolution. Assuming that EPTV only modulates the exact displacement field, the MTF is calculated by least-square fitting of the measured displacement with a sinusoidal function, leading to:

$$MTF\left(\frac{\lambda}{W}\right) = \frac{\sum_{i=1}^{n_p} u_i u_{t,i}}{\sum_{i=1}^{n_p} u_{t,i}^2} \qquad (10)$$

with n_p being the number of grid points and u_t being the true reference displacement, computed according to Eq. 9.

In Figure 2 the performances of the standard EPTV algorithm with isotropic and uniform weight, the enhanced version proposed by Agüera et al. [26] and the Adaptive EPTV are compared. The bin size b is set to 16 pixels for the only purpose of demonstration of the algorithm capabilities. This choice guarantees good convergence of the statistics, since the average number of particles per bin is ≈ 1280, according to Eq. 1 assuming square bins $b \times b$. The grid spacing is set to 1 pixels in the y direction to minimize effects of the approximation of the second derivative due to finite grid spacing. This approach is in line with the expected configuration in which this method will be used, where high-resolution of the statistics is sought and, expectedly, a small grid spacing is set. For the Adaptive EPTV, the predictor is built with the polynomial filtering approach of Agüera et al. [26] and the threshold to activate the stretching is set to $1/b^2$ as mentioned above.

The MTF is presented as a function of the normalized frequency, expressed as the ratio b/λ between the bin size and the wavelength of the sinusoidal displacement. The normalized frequency is varied between $b/0.1 = 160$ and $b/1.6 = 10$ pixels. For the standard EPTV and the enhanced version with polynomial fit, square averaging regions have been used. As expected, the MTF of the standard EPTV process follows the theoretical impulsive response of a top-hat filter, i.e. $sinc(b/\lambda)$. While for large

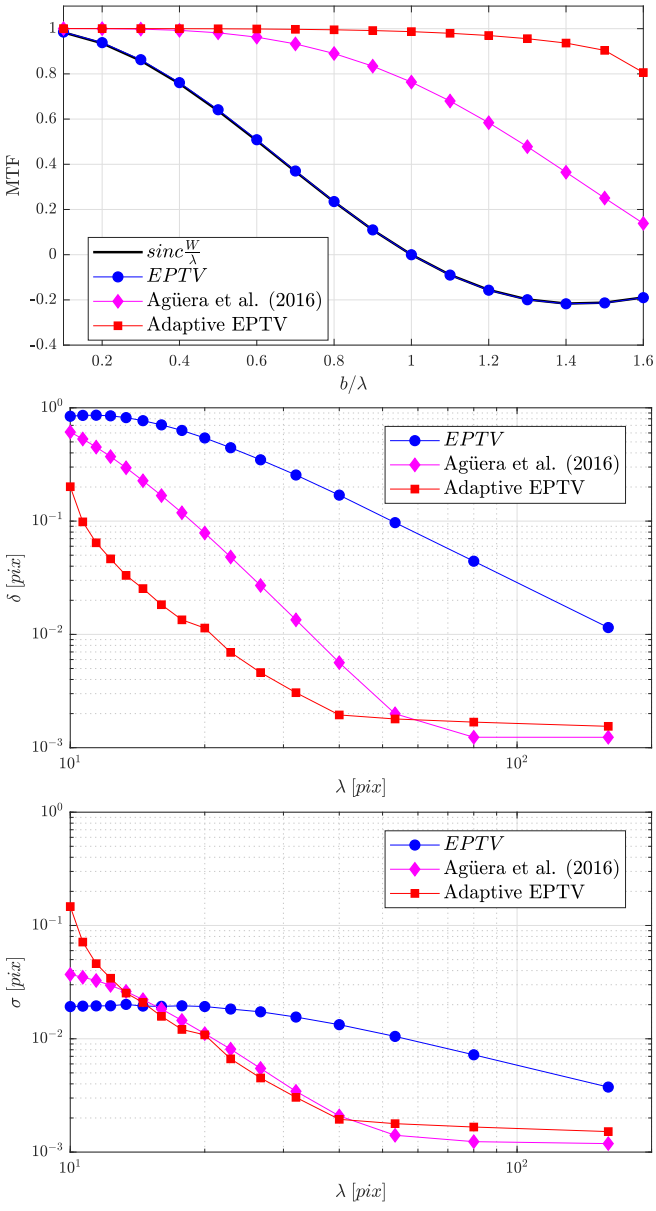

Figure 2. Modulation Transfer Function (top), total error (center) and random error (bottom) for the sinusoidal displacement test case for different wavelength λ. The bin size b is set to 16 *pix*.

wavelengths the Adaptive EPTV and the EPTV with polynomial fit [26] have similar performance, an evident enhancement of the MTF is observed for scales smaller than the bin size. At $b/\lambda = 1.5$, the MTF of the Adaptive EPTV is still around 0.91, while for the enhanced PTV with polynomial fit is approaching about 0.25. Clearly, for smaller wavelengths, the estimated predictor is not able to deliver a sufficiently accurate mapping of the second derivatives, thus hindering the bin stretching.

The accuracy is quantified in terms of total error δ and random error σ, defined respectively as:

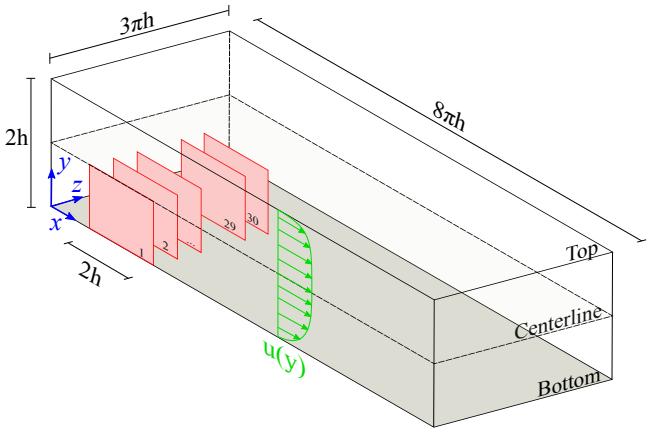

Figure 3. Sketch of the domain of the channel-flow database. Dimensions not in scale. The red squares indicate examples of region from which data are extracted to generate particle images.

$$\delta = \sqrt{\frac{1}{n_p}\sum_{i=1}^{n_p}(u_i - u_{t,i})^2} \tag{11}$$

$$\sigma = \sqrt{\frac{1}{n_p}\sum_{i=1}^{n_p}(u_i - MTF \cdot u_{t,i})^2} \tag{12}$$

Eq. 12 is again obtained by assuming that the EPTV process only modulates the exact displacement. Consequently, the random error can be measured by the deviation of the measured displacement field from an amplitude-modulated sinusoidal displacement field, with modulation equal to the MTF measured by Eq. 10. An insightful derivation of this formula is reported in [40].

Figure 2 reports the profiles of total (center) and random error (bottom) as a function of the wavelength. For the largest tested wavelength, the standard EPTV error is almost equally shared between total and random, while for Adaptive EPTV and the enhanced PTV with polynomial filtering the performances are similar up to a wavelength of approximately 50 pixels. For smaller wavelengths, the systematic error becomes the dominant share, with significant accuracy improvement when using the adaptive procedure.

It should be remarked that, while for the EPTV the random error is approximately constant for $\lambda < 2b$, both the Adaptive EPTV and the EPTV with polynomial filtering show an increase of the random error. This might be related to larger uncertainty in performing the Savitzky-Golay fitting of strongly spatially-variable displacements, and computing the corresponding second derivatives for the bin stretching.

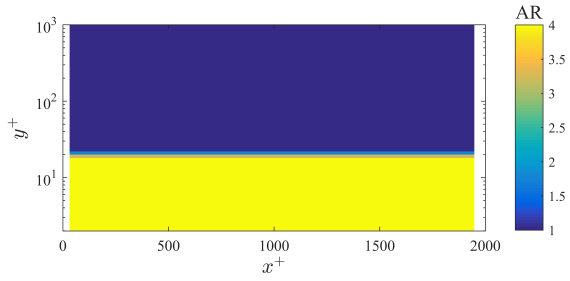

Figure 4. Aspect Ratio for the streamwise velocity component of the adapted averaging bins with 16x16 pixels windows. The x and y coordinates are normalized in inner units; y-axis is represented in logarithmic scales.

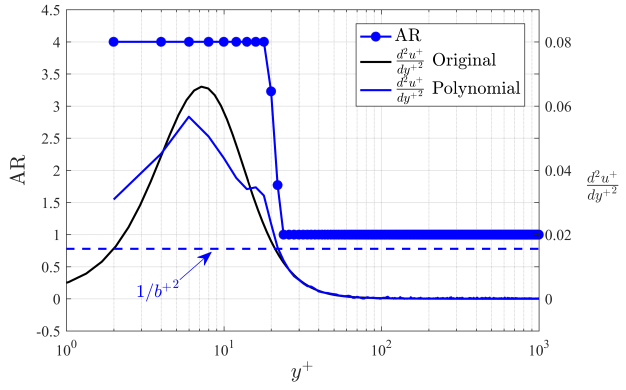

Figure 5. Streamwise-averaged crosswise profile of the aspect ratio of the adapted averaging bins with 16x16 pixels windows. The second derivative of the velocity field from both the original DNS velocity profile and from the EPTV with polynomial fitting is reported alongside. The horizontal dashed line represent the minimum threshold to activate the bin stretching. The y-axis is normalized in inner units and represented in logarithmic scales.

3.2. Channel flow

The algorithm has been further tested on a synthetic dataset based on flow simulations from the Johns Hopkins Turbulence Databases (JHTDB, `http://turbulence.pha.jhu.edu/`). This dataset represents a good benchmark for experiments in wall-bounded flows, where the presence of strong velocity gradients introduces significant systematic errors in the statistics. This error hinders the direct estimation, for instance, of the average wall-shear stress, which has a key role in determining friction drag. The synthetic test case is based on the dataset of direct numerical simulations in a channel at friction Reynolds number $Re_\tau \sim 1000$ [41, 42] with bulk velocity U_b equal to 1. The DNS domain spans 2 half-channel-heights h from wall to wall, $3\pi h$ in the span-wise direction and $8\pi h$ in the stream-wise direction. The DNS sequence duration is of one channel flow-through time $8\pi h/U_b$ with a DNS time step of $\delta t = 0.0013h/U_b$. This channel-flow dataset has been recently gaining popularity in the PIV community as a benchmark for processing algorithms [43].

To simulate a virtual 2D-PIV experiment, 2D velocity fields were extracted over a $h \times 2h$ domain (going from the wall to the centerline) in the $x - y$ plane, similarly to the synthetic test case reported in Ref. [44]. For each spatial location flow fields are extracted each 5 DNS time steps, thus providing 200 fields from the entire duration of the simulation. The flow fields are extracted at 30 different locations, separated of $0.2h$ in the z-direction. The 2D sub-domains extracted from the channel DNS are sketched in Figure 3. A set of 6000 image pairs is generated from the DNS flow fields. The images have size 500×1000 pixels, thus corresponding to a resolution of 0.5 pixels per wall unit. The particle image density is equal to 0.01 particles per pixel. The particle images are generated by the integration of randomly-distributed Gaussian spots with diameter equal to 2.5 pixels and maximum intensity of 100 counts.

The EPTV procedure has been applied to the set of synthetic images using averaging windows of 16×16 pixels. The predictor field fed to the PTV algorithm has been obtained using a multi-pass [1] image-deformation interrogation algorithm [2] with final windows size of 48×48 pixels.

The results are presented scaled in inner form, i.e. using the friction velocity $u_\tau = 0.0499$ and the viscosity $\nu = 5 \cdot 10^{-5}$ in the non-dimensional units of the DNS simulation. Inner-scaled quantities are indicated with the superscript $^+$.

Based on the EPTV results, stretched averaging bins have been obtained setting $AR_{max} = 4$, $\epsilon = 0.3$ and minimum value of the largest singular value to activate the stretching equal to $1/b^2$, as in the previous synthetic test case. Figure 4 shows the AR of the adapted averaging bins computed in this step. Since mean velocity differences are relevant only in the y-direction, the AR distribution results approximately in a step function which assumes value 4 when the second spatial derivative of the mean velocity profile in the y-direction is higher than $1/b^2$. These values of the wall-normal distance to activate the stretching depend on the size of the window itself due to the averaging effect of the EPTV process in building the predictor. In order to further stress out this point, Figure 5 compares the streamwise-averaged crosswise AR profile of the A-EPTV window and the velocity curvature in the y-direction. The latter is computed both from the velocity profile reported in the JHTDB for the channel database and from the polynomial-fitted EPTV estimation which has been fed to the adaptive algorithm. The minimum curvature $1/b^2$ which activates the stretching (in horizontal dashed line) is reported as well for the 16×16 pixels window case. The point where the stretching is activated

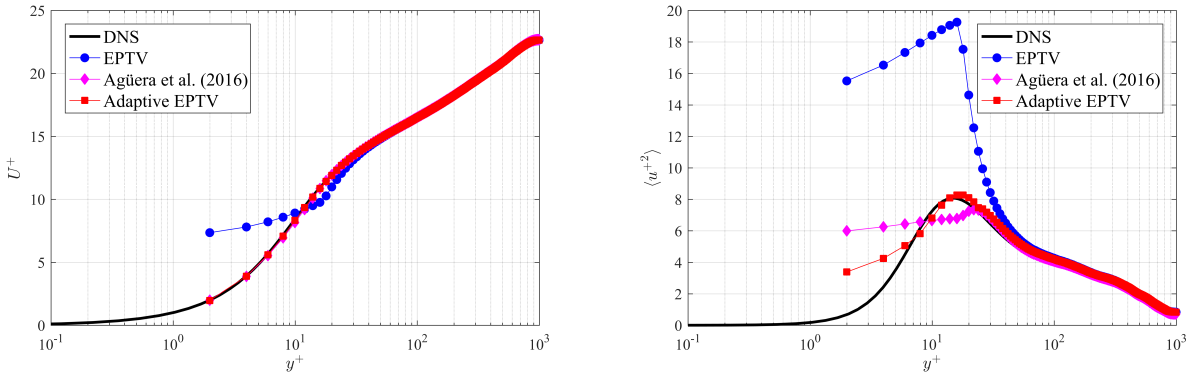

Figure 6. Statistics for the turbulent channel flow test case. Left: profile of average streamwise velocity component for 16x16 pixels windows. Right: profile of the variance of the streamwise velocity component for 16x16 pixels windows. The results are presented scaled in inner units.

by the threshold $d^2u^+/dy^{+2} > 1/b^{+2}$ corresponds to $y^+ < 22$ (with b^+ being the interrogation window size expressed in inner units).

In Figure 6, the performances of the adaptive algorithm are compared in terms of profiles of streamwise average velocity and velocity fluctuations against both the ground truth, i.e. the original profile from the DNS dataset, and isotropic-window EPTV methods. The adaptive EPTV and the EPTV procedure by Agüera et al. [26] are capable of accurately follow the DNS average velocity profile up to 2 wall units from the wall. This is equivalent to 1 pixel, which is the grid spacing selected for this test. The standard EPTV procedure, instead, offers a good estimation of the velocity profile up to 30 wall units, i.e. up to $y \approx b$. The standard EPTV procedure provides also the worst estimation of the velocity fluctuation profile, following accurately the DNS profile up to $y^+ = 46$. The Adaptive EPTV procedure and the EPTV with local polynomial fitting described by Agüera et al. [26] shows similar performances for $y^+ > 22$, i.e. when the adaptive algorithm uses windows with $AR = 1$. Closer to the wall the adaptive algorithm shows an improvement with respect to the EPTV with local polynomial fitting in the estimation of the fluctuation profile, following accurately the DNS up to $y^+ = 8$. The EPTV with local polynomial fitting, instead, is accurate up to $y^+ = 16$. It is worth highlighting that both the Adaptive EPTV and the EPTV with local polynomial fitting are able to provide estimations of the flow statistics with great accuracy up to wall-distances at least up to half of the averaging bin height.

3.3. Flow around a NACA0012 airfoil

In the previous validation tests the optimal stretching direction was trivial, since the only relevant second derivative was $\partial^2 u/\partial y^2$. In addition to this, due to the absence of (or very limited for the channel flow)

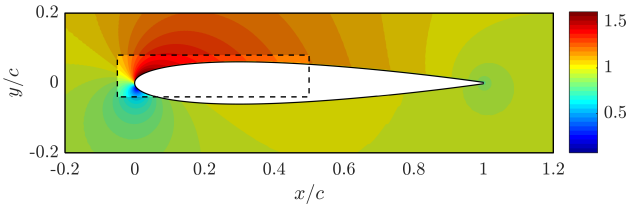

Figure 7. Contour of the velocity magnitude of the reference field. The highlighted region corresponds to the area depicted in Figure 8.

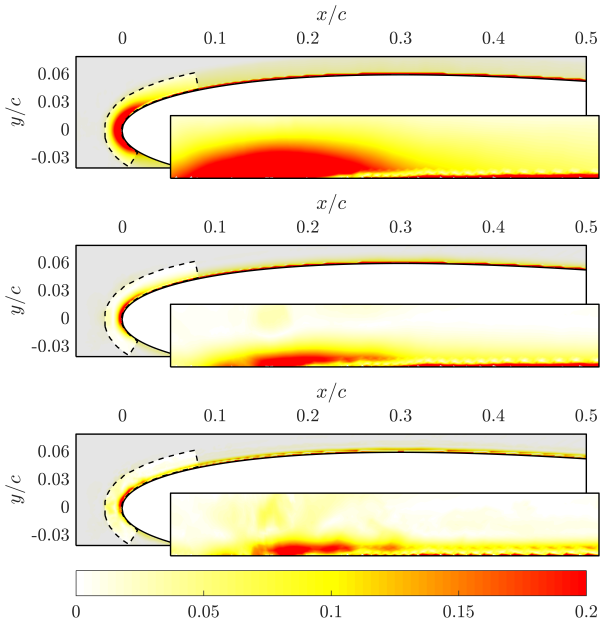

Figure 8. Contour of the error magnitude (Right column) in a inset close to the leading edge for (from top to bottom) standard EPTV, EPTV with local polynomial fitting and the proposed Adaptive EPTV. The inset shows the error map in curvilinear coordinates around the leading edge.

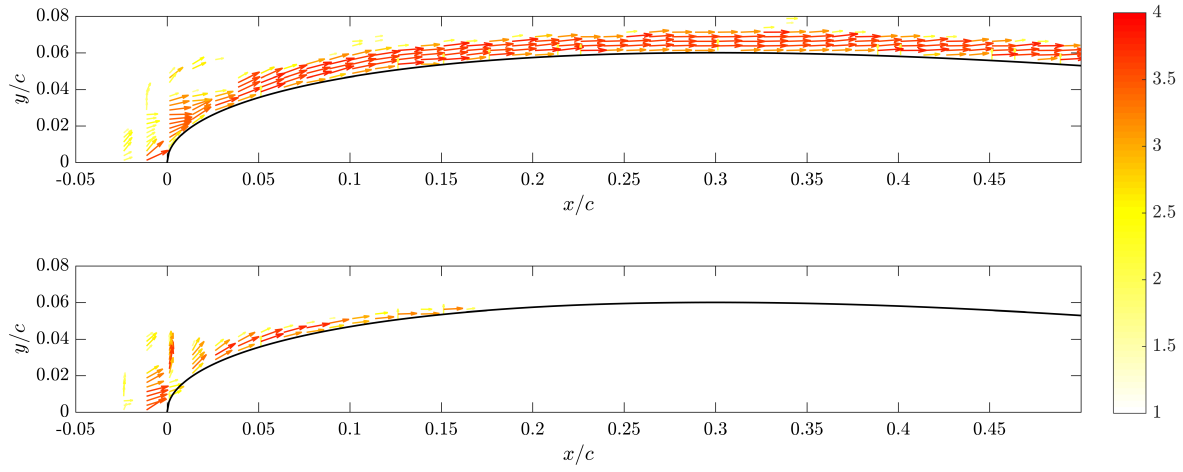

Figure 9. Principal direction vector plot of the stretched window for the streawmise (top row) and crosswise (bottom row) velocity components. The arrow color corresponds to the aspect ratio of the stretching. The magnitude of the vectors is scaled directly with the local aspect ratio of the stretched windows. The arrows are plotted every 10 vectors and every 2 vectors in the streamwise and crosswise directions, respectively.

gradients in the direction orthogonal to the curvature, a uniformly stretched window would have provided similar results to the proposed adaptive algorithm.

In this section, the performances of the adaptive algorithm are demonstrated in a condition in which the principal directions of the curvature of the displacement field are space-dependent, thus requiring different stretching ratios and orientations of the averaging bins.

The synthetic test case presented in this section is based on the flow field around a NACA0012 airfoil at chord-based Reynolds number equal to $1 \cdot 10^7$ and at angle of attack of 5 deg. The average flow field is obtained with XFOIL [45]. The airfoil is discretized using 160 panels. Free laminar-turbulent transition of the boundary layer is calculated using the e^N method with $N = 9$, resulting in a transition at $x/c = 0.05$ on the suction side and at $x/c = 0.75$ on the pressure side. The velocity magnitude contours of the XFOIL flow field are reported in Figure 7 for reference.

A set of 1000 images is generated with a procedure similar to the previous synthetic test case. A domain of 0.5×1.5 chords c is discretized with 400×1000 pixels, i.e. 800 pixels/c. The particle image density and characteristics (intensity, diameter, etc.) are the same of the previous test case. The averaging is carried out on bins of 32×32 pixels, thus resulting in about 10^4 particles per bin. The relatively large size of the averaging bin is adopted to create a test case representative of the limitations of 3D experiments as discussed in Sec. 1.

It is worth to remark here, that the virtual PIV images have been generated only taking into account the mean flow field, i.e. turbulent fluctuations are not simulated. As in the previous test cases, averaging bins have been obtained setting $AR_{max} = 4$, $\epsilon = 0.3$ and threshold to activate the stretching equal to $1/b^2$ (with $b = 32$ pixels).

Figure 8 shows the error magnitude for the standard EPTV, the polynomial-fitted EPTV and the Adaptive EPTV over a portion of the field including the leading edge (as highlighted in Figure 7). The error has been computed as $\varepsilon = \sqrt{(u-u_t)^2 + (v-v_t)^2}$, where u and v are respectively the streamwise and crosswise velocity, and u_t, v_t indicate the velocity field of the ground truth. An inset reporting the error map in curvilinear coordinates around the leading edge is reported to highlight the differences. The average error computed only in the inset and normalized with the freestream velocity is equal to 10.2%, 3.8% and 3.5% for the standard EPTV, the EPTV with local polynomial filtering and the proposed Adaptive EPTV, respectively.

For the standard EPTV process the largest errors are achieved in the flow acceleration region close to the leading edge, as shown in the inset of Figure 8. In general, the standard EPTV process is challenged by the strong flow acceleration along the entire first portion of the suction side, and by the strong velocity gradients close to the airfoil surface.

The EPTV with local polynomial filtering achieves already a significant improvement due to its ability to cope with strong local velocity gradients. The proposed Adaptive EPTV method shows slightly larger errors close to the leading edge if compared with the local polynomial fitting, possibly due to inaccuracy in

the estimation of the principal directions of the Hessian matrix. Nonetheless, throughout the suction side a reduction of the error level close to the airfoil surface is achieved.

The Aspect Ratio and the corresponding principal direction of stretching for the streamwise and crosswise velocity components are presented in Figure 9. As expected, the bin stretching for the u component is particularly evident on the suction side, where the flow exhibits the strongest accelerations. For the v component the stretching is activated only in proximity of the leading edge and the trailing edge.

4. Experimental application to impinging jet with fractal grids

The Adaptive EPTV algorithm is tested on an experimental test case for validation on real data. The flow field of the jet issued from a nozzle equipped with a fractal grid as turbulator is analyzed. The experiments are carried out in the air jet facility at the University of Naples Federico II. Air is collected from the environment with a centrifugal blower; an inverter is used to regulate the input shaft power. The flow rate is measured using a rotameter, then the fluid passes through a radiator to control it in temperature and it is then collected within a stagnation chamber (internal diameter and length equal to $3D$ and $20D$, respectively, being $D = 20$ mm) located upstream of the nozzle. Two honeycomb grids are located within the stagnation chamber to abate any large-scale fluctuation generated in the feeding circuit. A contoured nozzle is used to carry the airflow through a short-pipe ($6.2D$ long) characterized by a round exit section; a terminating cap is located in correspondence of the nozzle exit section to allow for the accurate positioning of the grid (Figure 10).

The stagnation chamber and the nozzle are arranged on a traversing stage allowing for the displacement along the nozzle axis direction. A glass square impinging plate is located at a fixed distance $X = 2D$ from the nozzle exit section. The size of the glass plate ($15D \times 15D$) is chosen so that boundary effects on the flow field are negligible. The accuracy on the nozzle-to-plate distance is of the order $1/20D$.

Here and in the following X and Y indicate the streamwise and lateral coordinate, respectively; correspondingly, U and V indicate the velocity components in the X and Y directions. The lower case u^2 is used to indicate the variance of the streamwise velocity.

The flow is seeded with olive oil particles (about $1\,\mu$m diameter) generated using a Laskin nozzle. The mixing between the working fluid and the seeding particles occurs in a reservoir located upstream of the stagnation chamber. The light source is a Quantel Evergreen laser (532 nm wavelength, 200 mJ/pulse; $\leq$ 10 ns pulse duration) with an exit beam diameter of about 5 mm. The PIV imaging system consists of one Andor Zyla sCMOS 5.5 Mpixels. The camera is aligned such that it results orthogonal to the laser sheet and equipped with a 100 mm Tokina objective, with focal aperture set to $f_{\#} = 16$. The imaged area covers $2D$ in the streamwise (X) direction and $2.5D$ in the lateral direction, thus resulting in a spatial resolution of 50 pix/mm. The acquisition frequency is set to 15 Hz. The laser is operated in dual-pulse mode, with time delay between the two pulses of $16\mu s$. The flow rate is regulated using the rotameter in order to obtain a Reynolds number (based on the nozzle exit section diameter D) equal to $Re = 15,000$. The resulting bulk velocity is then $U_b = 11$ m/s.

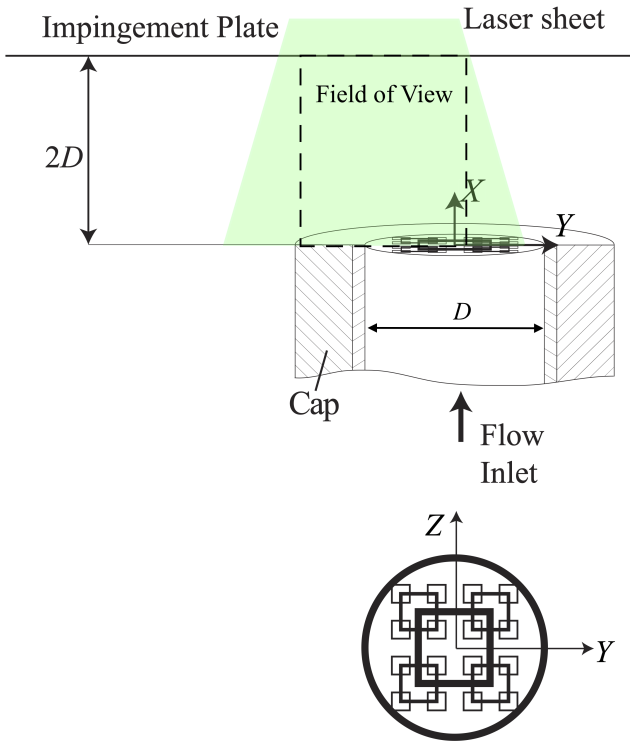

Figure 10. Schematic representation of the impinging jet rig facility.

The fractal grid employed for this experimental validation has already been studied for heat transfer enhancement purposes [46]. The length L_0 and the thickness t_0 of the first iteration of the investigated square fractal grid are equal to 10 mm and 1 mm, respectively. The grid is characterized by three iterations; at each iteration j the length L_j and the thickness t_j are halved, i.e. $L_j = L_0 R_L^j$ and $t_j = t_0 R_t^j$, with $R_L = R_t = 1/2$. For this grid the ratio between the largest and the smallest bar thickness (i.e. the thickness ratio t_r) is equal to 4. The blockage ratio of

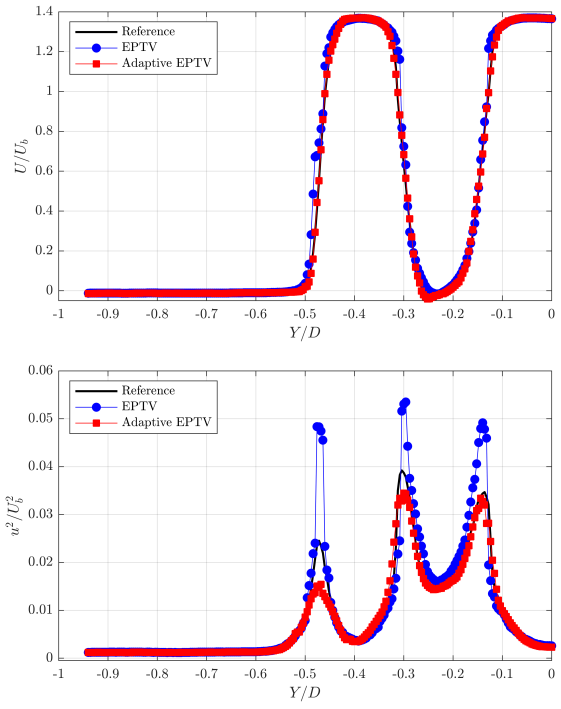

Figure 11. Statistics for the turbulent fractal jet test case. Top: profile of mean streamwise velocity component normalised with respect to the bulk streamwise velocity U_b. Bottom: profile of the variance of the streamwise velocity component normalised with respect to U_b^2. The profiles are taken at $X/D = 0.2$.

the grid is equal to 0.32.

The choice of the fractal pattern was driven by the peculiar features in terms of turbulence production that were demonstrated in wind tunnel experiments [47]. Differently from the canonical ones, fractal grids show a more elongated production region; more importantly, the location of the peak is related to the grid geometry [48], making them particularly amenable for practical applications. The flow field obtained when placing a fractal grid insert in correspondence of the round jet exit section was described in the case of free [49] and impinging jets [50]. In both cases, the existence of a strong interaction among jet-like and wake-like behaviour significantly challenges the accuracy of the capabilities of the PIV algorithm, requiring a large dynamic range.

A set of 200 snapshots is processed using a standard EPTV algorithm and the Adaptive EPTV, with interrogation window size of 64×64 pixels grid with 4 pixels grid spacing. The reference flow statistics are obtained with a larger dataset of 2000 samples, allowing excellent convergence using a standard EPTV with window size of 16×16 pixels and the same grid spacing of 4 pixels (i.e. 75% overlap). The choice of a final interrogation spot of 64×64, which is far from the desired resolution when using EPTV, is driven indeed by the need of building with the available images a reference field with significantly higher spatial resolution and robust statistical convergence. The large interrogation window helps in reaching fast convergence also on the reduced subset of 200 images.

The particle pairs are built similarly to the previous test case, using a super-resolution [18] PIV with multi-pass [1] image deformation algorithm [2] with final window size of 40×40 pixels and 75% overlap.

Figure 11 reports the profiles of the mean streamwise velocity and of the streamwise normal velocity variance at the location $X/D = 0.2$. As already mentioned, the fractal impinging jet represents a challenging flow field for the PIV algorithm due to the strong interaction of jet-like and wake-like regions, which in turn generate intense shear layers. In particular, the U/U_b profile measured at $X/D = 0.2$ features a strong low momentum region in the lee of the first iteration grid bars. The streamwise normalised velocity exceeds 1 as a consequence of the blockage ratio of the grid (which is 32%). The bulk velocity is indeed based on the mass flow rate measured by the rotameter. When the grid is placed in correspondence of the nozzle exit section, the flow emerging through the holes experiences a significant acceleration as a consequence of the reduced effective area. The streamwise velocity is then suddenly reduced from $U/U_b \approx 1.4$ to 0. An overall view of the mean streamwise velocity field is reported in Figure 12. The three processes seem to lead to qualitatively similar results (as also evidenced in Figure 12). Nonetheless, significant differences are observed from a quantitative analysis. Figure 13 reports the normalized differences between the EPTV and the A-EPTV algorithm with respect to the reference flow field for the mean streamwise velocity and for the variance of the streamwise velocity. In the shear layer region, both mean and variance estimated using the EPTV algorithm show signficant discrepancies with respect to the reference flow field.

Conversely, the Adaptive EPTV algorithm follows more closely the reference profile, showing no significant differences on the mean flow and only little overestimate of the variance in the outer shear layer.

Figure 14 shows the regions where the A-EPTV algorithm introduces interrogation windows with aspect ratio different from 1 for the streamwise (a) and lateral (b) velocity components, respectively. The region corresponding to both the inner and outer shear layers requires the largest values of AR, thus leading to better resolved mean flow gradients. Furthermore, at X/D=2, in the region where the flow is characterized by the conversion of streamwise momentum into lateral one, the algorithm adapts the interrogation window aspect ratio to accurately measure the strong lateral

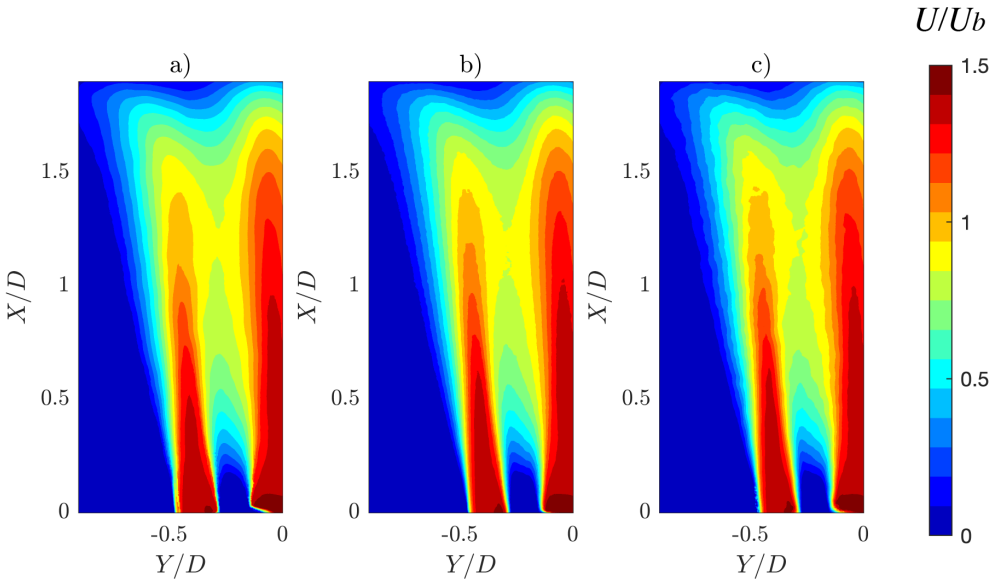

Figure 12. Spatial distribution of the mean streamwise velocity in the case of EPTV (a), Adaptive EPTV (b) and Reference (c).

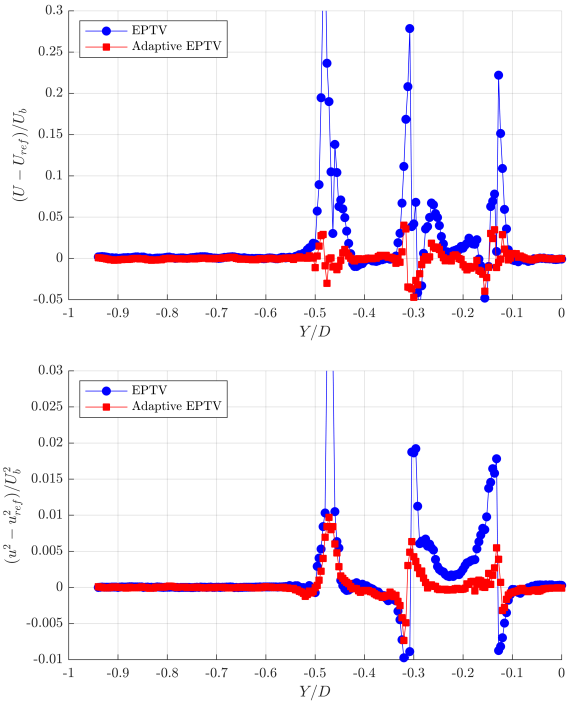

Figure 13. Statistics for the turbulent fractal jet test case. Top: difference between the mean streamwise velocity component obtained with the EPTV and the A-EPTV algorithm and the reference flow field (U_{ref}); data are normalised with respect to the bulk velocity U_b. Bottom: difference between the variance of the streamwise velocity component obtained with the EPTV and the A-EPTV algorithm and the reference flow field (u^2_{ref}) normalised with respect to U_b^2. The profiles are taken at $X/D = 0.2$.

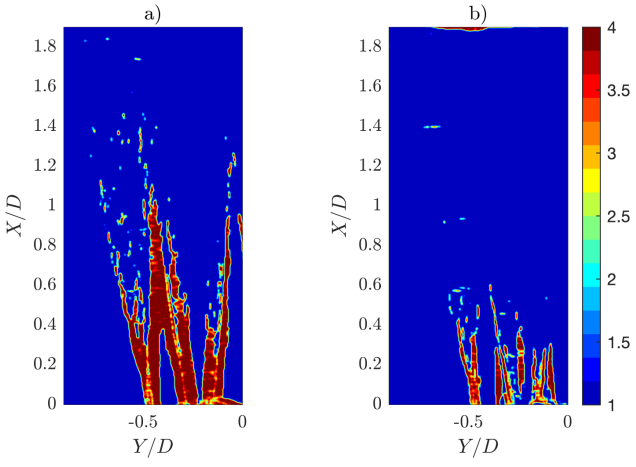

Figure 14. Aspect Ratio based on the Hessian of the streamwise (a) and lateral (b) velocity components of the adapted averaging bins with 16x16 pixels windows.

velocity gradients.

5. Conclusions

An adaptive principle to improve the spatial resolution of ensemble PTV is proposed. Complying with the idea that the main source of systematic errors in PIV is due to the velocity curvature, the averaging regions are stretched and oriented along the direction of maximum curvature. While for instantaneous measurement this adaptivity principle is hindered by noise amplification when computing second derivatives, its application is shown to be robust for mean flow fields computed from

EPTV.

The results of the validation with synthetic images and experimental data have demonstrated that a significant improvement of the spatial resolution can be achieved with this adaptivity principle. While this idea has been often used by manual selection of the stretched bins when the choice is trivial to be set *a priori* (for instance in turbulent boundary layers developing on flat plates), the proposed method automatically optimizes the local bin stretching. The only user input is the area of the averaging bin, which is set by the desired convergence constraint.

It has to be remarked that the Adaptive EPTV *per se* does not improve the convergence, which is solely dependent on the number of particles per bin. The clear advantage is that a larger bin can be used without penalizing the resolution, thus in this sense speeding up the convergence at fixed desired resolution level if compared to standard EPTV. Notice that in 3D applications a larger improvement is foreseeable, thanks to the possibility of exploiting the full 3D curvature information. The extension to 3D of the algorithm is trivial and already described in this work (Eqs. 4-8). The Adaptive EPTV allows reducing significantly the number of samples required to reach a certain spatial resolution, feature that is extremely desirable in 3D experiments, where due to the relatively low seeding concentration (both due to low image density to reduce reconstruction artifacts and due to the extension of the observation region in the third dimension) performing EPTV with high resolution might be unfeasible due to technical limitations.

Furthermore, the adaptive EPTV has shown to work very effectively when local polynomial fitting by Agüera et al [26] is employed, which allows high-resolution velocity predictors for bin stretching. Since the bin stretching compensates for the velocity curvature, the local polynomial fitting is still to be included in the process to suppress the detrimental effect of the residual velocity gradient on turbulent statistics.

Acknowledgements

MR and SD were partially supported by the Grant DPI2016-79401-R funded by the Spanish State Research Agency (SRA) and European Regional Development Fund (ERDF).

References

[1] J Soria. An investigation of the near wake of a circular cylinder using a video-based digital cross-correlation particle image velocimetry technique. *Experimental Thermal and Fluid Science*, 12(2):221–233, 1996.

[2] F Scarano. Iterative image deformation methods in PIV. *Measurement science and technology*, 13(1):R1, 2001.

[3] R Theunissen, F Scarano, and ML Riethmuller. An adaptive sampling and windowing interrogation method in PIV. *Measurement Science and Technology*, 18(1):275–287, 2007.

[4] T Astarita. Adaptive space resolution for PIV. *Experiments in Fluids*, 46(6):1115–1123, 2009.

[5] M Novara, A Ianiro, and F Scarano. Adaptive interrogation for 3D-PIV. *Measurement Science and Technology*, 24(2), 2013.

[6] A Sciacchitano, F Scarano, and B Wieneke. Multi-frame pyramid correlation for time-resolved PIV. *Experiments in Fluids*, 53(4):1087–1105, 2012.

[7] R Hain and CJ Kähler. Fundamentals of multiframe particle image velocimetry (PIV). *Experiments in Fluids*, 42(4):575–587, 2007.

[8] J Schneiders and F Scarano. Dense velocity reconstruction from tomographic PTV with material derivatives. *Experiments in Fluids*, 57(9):139, 2016.

[9] CD Meinhart, ST Wereley, and JG Santiago. A PIV algorithm for estimating time-averaged velocity fields. *Journal of Fluids Engineering*, 122(2):285–289, 2000.

[10] J Westerweel, PF Geelhoed, and R Lindken. Single-pixel resolution ensemble correlation for micro-PIV applications. *Experiments in Fluids*, 37(3):375–384, 2004.

[11] CJ Kähler, U Scholz, and J Ortmanns. Wall-shear-stress and near-wall turbulence measurements up to single pixel resolution by means of long-distance micro-piv. *Experiments in fluids*, 41(2):327–341, 2006.

[12] S Scharnowski, R Hain, and CJ Kähler. Reynolds stress estimation up to single-pixel resolution using PIV-measurements. *Experiments in Fluids*, 52(4):985–1002, 2012.

[13] F Billy, L David, and G Pineau. Single pixel resolution correlation applied to unsteady flow measurements. *Measurement Science and Technology*, 15(6):1039, 2004.

[14] U Scholz and CJ Kähler. Dynamics of flow structures on heaving and pitching airfoils. In *13th International Symposium of Laser Techniques to Fluid Mechanics*, 2006.

[15] F Avallone, S Discetti, T Astarita, and G Cardone. Convergence enhancement of single-pixel PIV with symmetric double correlation. *Experiments in Fluids*, 56(4):71, 2015.

[16] S Discetti and F Coletti. Volumetric velocimetry for fluid flows. *Measurement Science and Technology*, 29(4):042001, 2018.

[17] EA Cowen and SG Monismith. A hybrid digital particle tracking velocimetry technique. *Experiments in Fluids*, 22(3):199–211, 1997.

[18] RD Keane, RJa Adrian, and Z Yuanhui. Super-resolution particle imaging velocimetry. *Measurement Science and Technology*, 6(6):754, 1995.

[19] B Wieneke. Iterative reconstruction of volumetric particle distribution. *Measurement Science and Technology*, 24(2):024008, 2012.

[20] D Schanz, S Gesemann, and A Schröder. Shake-the-box: Lagrangian particle tracking at high particle image densities. *Experiments in Fluids*, 57(5):70, 2016.

[21] CJ Kähler, S Scharnowski, and C Cierpka. On the resolution limit of digital particle image velocimetry. *Experiments in Fluids*, 52(6):1629–1639, 2012.

[22] LP Chamorro, DR Troolin, SJ Lee, REA Arndt, and F Sotiropoulos. Three-dimensional flow visualization in the wake of a miniature axial-flow hydrokinetic turbine. *Experiments in Fluids*, 54(2):1459, 2013.

[23] A Schröder, D Schanz, D Michaelis, C Cierpka, S Scharnowski, and CJ Kähler. Advances of PIV and 4D-

PTV "shake-The-Box" for Turbulent Flow Analysis -the Flow over Periodic Hills. *Flow, Turbulence and Combustion*, 95(2-3):193–209, 2015.

[24] JF Schneiders, F Scarano, and GE Elsinga. Resolving vorticity and dissipation in a turbulent boundary layer by tomographic PTV and VIC+. *Experiments in Fluids*, 58(4):27, 2017.

[25] JF Schneiders, F Scarano, C Jux, and A Sciacchitano. Coaxial volumetric velocimetry. *Measurement Science and Technology*, 29(6):065201, 2018.

[26] N Agüera, G Cafiero, T Astarita, and S Discetti. Ensemble 3D PTV for high resolution turbulent statistics. *Measurement Science and Technology*, 27(12), 2016.

[27] M Novara, D Schanz, N Reuther, CJ Kähler, and A Schröder. Lagrangian 3D particle tracking in high-speed flows: Shake-The-Box for multi-pulse systems. *Experiments in Fluids*, 57(8):128, 2016.

[28] C Sanmiguel Vila, R Örlü, R Vinuesa, P Schlatter, A Ianiro, and S Discetti. Adverse-pressure-gradient effects on turbulent boundary layers: statistics and flow-field organization. *Flow, turbulence and combustion*, 99(3-4):589–612, 2017.

[29] D Di Florio, F Di Felice, and GP Romano. Windowing, re-shaping and re-orientation interrogation windows in particle image velocimetry for the investigation of shear flows. *Measurement Science and Technology*, 13(7):953, 2002.

[30] F Scarano. Theory of non-isotropic spatial resolution in PIV. *Experiments in Fluids*, 35(3):268–277, 2003.

[31] R Theunissen, F Scarano, and ML Riethmuller. Spatially adaptive PIV interrogation based on data ensemble. *Experiments in Fluids*, 48(5):875–887, 2010.

[32] H Nobach, N Damaschke, and C Tropea. High-precision sub-pixel interpolation in particle image velocimetry image processing. *Experiments in Fluids*, 39(2):299–304, 2005.

[33] C Cierpka, R Segura, R Hain, and CJ Kähler. A simple single camera 3C3D velocity measurement technique without errors due to depth of correlation and spatial averaging for microfluidics. *Measurement Science and Technology*, 21(4):045401, 2010.

[34] K Nishino, N Kasagi, and M Hirata. Three-dimensional particle tracking velocimetry based on automated digital image processing.

[35] CE Willert and M Gharib. Three-dimensional particle imaging with a single camera. *Experiments in Fluids*, 12(6):353–358, 1992.

[36] A Schröder, R Geisler, K ét al al Staack, GE Elsinga, F Scarano, B Wieneke, A Henning, C Poelma, and J Westerweel. Eulerian and Lagrangian views of a turbulent boundary layer flow using time-resolved tomographic PIV. *Experiments in Fluids*, 50(4):1071–1091, 2011.

[37] M Novara and F Scarano. A particle-tracking approach for accurate material derivative measurements with tomographic PIV. *Experiments in Fluids*, 54(8):1584, 2013.

[38] N Mordant, AM Crawford, and E Bodenschatz. Experimental lagrangian acceleration probability density function measurement. *Physica D: Nonlinear Phenomena*, 193(1-4):245–251, 2004.

[39] NT Ouellette, H Xu, and E Bodenschatz. A quantitative study of three-dimensional lagrangian particle tracking algorithms. *Experiments in Fluids*, 40(2):301–313, 2006.

[40] T Astarita. Analysis of interpolation schemes for image deformation methods in PIV: effect of noise on the accuracy and spatial resolution. *Experiments in Fluids*, 40(6):977–987, 2006.

[41] Y Li, E Perlman, M Wan, Y Yang, C Meneveau, R Burns, S Chen, A Szalay, and G Eyink. A public turbulence database cluster and applications to study lagrangian evolution of velocity increments in turbulence. *Journal of Turbulence*, (9):N31, 2008.

[42] H Yu, K Kanov, E Perlman, J Graham, E Frederix, R Burns, A. Szalay, G. Eyink, and C. Meneveau. Studying lagrangian dynamics of turbulence using on-demand fluid particle tracking in a public turbulence database. *Journal of Turbulence*, (13):N12, 2012.

[43] CJ Kähler, T Astarita, PP Vlachos, J Sakakibara, R Hain, S Discetti, R La Foy, and C Cierpka. Main results of the 4th International PIV Challenge. *Experiments in Fluids*, 57(6):97, 2016.

[44] M Raiola, S Discetti, and A Ianiro. On PIV random error minimization with optimal POD-based low-order reconstruction. *Experiments in Fluids*, 56(4):75, 2015.

[45] M Drela. XFOIL: An analysis and design system for low Reynolds number airfoils. In *Low Reynolds number aerodynamics*, pages 1–12. Springer, 1989.

[46] G Cafiero, S Discetti, and T Astarita. Heat transfer enhancement of impinging jets with fractal-generated turbulence. *International Journal of Heat and Mass Transfer*, 75:173–183, aug 2014.

[47] D Hurst and JC Vassilicos. Scalings and decay of fractal-generated turbulence. *Physics of Fluids*, 2007.

[48] N Mazellier and JC Vassilicos. Turbulence without Richardson-Kolmogorov cascade. *Physics of Fluids*, 2010.

[49] G Cafiero, S Discetti, and T Astarita. Flow field topology of submerged jets with fractal generated turbulence. *Physics of Fluids*, 27(11), 2015.

[50] G Cafiero, C S Greco, T Astarita, and S Discetti. Flow field features of fractal impinging jets at short nozzle to plate distances. *Experimental Thermal and Fluid Science*, 78:334–344, 2016.